Evaluation of ITER divertor shunts as a synthetic diagnostic for detachment control

Document status and date:
Published: 01/08/2023

Document Version:
Publisher's PDF, also known as Version of Record (includes final page, issue and volume numbers)

Please check the document version of this publication:

• A submitted manuscript is the version of the article upon submission and before peer-review. There can be important differences between the submitted version and the official published version of record. People interested in the research are advised to contact the author for the final version of the publication, or visit the DOI to the publisher's website.
• The final author version and the galley proof are versions of the publication after peer review.
• The final published version features the final layout of the paper including the volume, issue and page numbers.

Link to publication

PAPER • OPEN ACCESS

Evaluation of ITER divertor shunts as a synthetic diagnostic for detachment control

To cite this article: C.A. Orrico *et al* 2023 *Nucl. Fusion* **63** 086002

View the article online for updates and enhancements.

Evaluation of ITER divertor shunts as a synthetic diagnostic for detachment control

C.A. Orrico[1,2] ⓘ**, T. Ravensbergen**[2,*] ⓘ**, R.A. Pitts**[2] ⓘ**, X. Bonnin**[2]**, E. Kaveeva**[3] ⓘ**, J.S. Park**[4] ⓘ**, V. Rozhansky**[3]**, I. Senichenkov**[3] ⓘ**, C. Watts**[2] **and M. de Baar**[1,5]

[1] Eindhoven University of Technology, Department of Mechanical Engineering, Control Systems Technology Group, PO Box 513, 5600 MB Eindhoven, Netherlands
[2] ITER Organization, Route de Vinon-sur-Verdon, CS 90 046, 13067 St. Paul Lez Durance Cedex, France
[3] Peter the Great St. Petersburg Polytechnic University, Polytechnicheskaya 29, 195251 St. Petersburg, Russian Federation
[4] Oak Ridge National Laboratory, Oak Ridge, TN 37831, United States of America
[5] Dutch Institute for Fundamental Energy Research, De Zaale 20, 5612 AJ Eindhoven, Netherlands

E-mail: Timo.Ravensbergen@iter.org

Abstract

Reliable diagnostics that measure the detached state of the ITER divertor plasma will be necessary to control heat flux to the divertor targets during steady state, burning plasma operation. This paper conducts an initial exploration into the feasibility of the divertor shunt diagnostic as a lightweight, robust, and real-time detachment sensor. This diagnostic is a set of shunt lead pairs that measure the voltage drop along the divertor cassette body, from which the plasma scrape-off layer (SOL) current is calculated. Using SOLPS-ITER simulations for control-relevant ITER plasma scenarios, the thermoelectric current magnitude along the SOL is shown to decrease significantly with the onset of partial detachment at the outer divertor target. Electromagnetic modelling of a simplified divertor cassette is used to develop a control-oriented inductance-resistance circuit model, from which SOL currents can be calculated from shunt pair voltage measurements. The sensitivity and frequency-response of the resulting system indicates that the diagnostic will accurately measure SOL thermoelectric currents during ITER operation. These currents will be a good measure of the detached state of the divertor plasma, making the divertor shunt diagnostic a potentially extremely valuable and physically robust sensor for real-time detachment control.

Keywords: plasma control, detachment, synthetic diagnostics, divertor, exhaust, SOLPS-ITER

(Some figures may appear in colour only in the online journal)

* Author to whom any correspondence should be addressed.

1. Introduction

An outstanding challenge facing ITER stationary plasma operation will be reduction of heat loads to the actively cooled tungsten (W) divertor targets [1, 2]. During baseline $Q_{DT} = 10$ fusion power operation in ITER, approximately 100 MW of power will be exhausted through the scrape-off layer (SOL) [1]. At most, $\simeq 10\%$ of the power will be deposited on the main chamber walls, with the remainder to be handled in the divertor. Only through volumetric power dissipation in the divertor plasma (achieved by radiation resulting from the injection of external seed impurities, e.g; neon (Ne)), leading to a partially detached divertor state, can heat loads to the targets be maintained below technologically manageable levels [1–4]. Any loss of detachment under these conditions will rapidly lead to peak heat fluxes in the range of several tens of MW m^{-2}.

Exceeding the power handling limits of the W monoblocks comprising the divertor targets will drive erosion of the W monoblock top surfaces and, in the worst case of plasma reattachment, lead to potential rupture of cooling channels [1]. This issue is particularly acute on ITER both as a consequence of the very high SOL powers and the divertor target design, which must use target tilting and monoblock surface shaping to hide the leading edges between toroidally neighbouring discrete components [1]. These geometrical factors considerably increase heat loads compared with cylindrically symmetric surfaces (by reducing wetted areas) in the case of plasma reattachment. The effects of plasma drifts are also predicted to strongly increase the inner-outer target peak heat load asymmetries in the case of divertor reattachment [1, 5, 6], further exacerbating the problem. It will therefore be crucial to provide a reliable means of real-time detachment control for ITER.

Several diagnostics suitable for detachment control will be available on ITER, though the field is still in relative infancy with regard to application on current tokamaks. Potential options include the real-time use of bolometry, filtered visible and infrared light imaging, neutral pressure gauges, various spectroscopic systems, and Langmuir probes [7, 8]. An additional system, referred to as the divertor shunt diagnostic will also be installed on several of the ITER divertor cassette It was originally designed to measure halo and vessel currents during vertical displacement events and to measure SOL currents during stationary plasma operation (with the divertor acting as a conductor to complete the poloidal SOL current circuit). Until now, however, the system has never been carefully studied with regard to deployment as a detachment state sensor on ITER. Experiments ASDEX Upgrade (AUG) were the first to demonstrate the power of such shunt diagnostics for tokamak detachment control [9] and this has now become a routine technique on the device. However, the AUG system is a more direct measurement, using a shunt resistance embedded in the divertor tile mounting, an approach not possible on ITER due to the more complex, actively cooled divertor.

As shown in figure 1, the shunt diagnostic consists of eight shunt lead pairs intended to measure the voltage drop along the ITER divertor cassette body. Of the 54 cassettes comprising
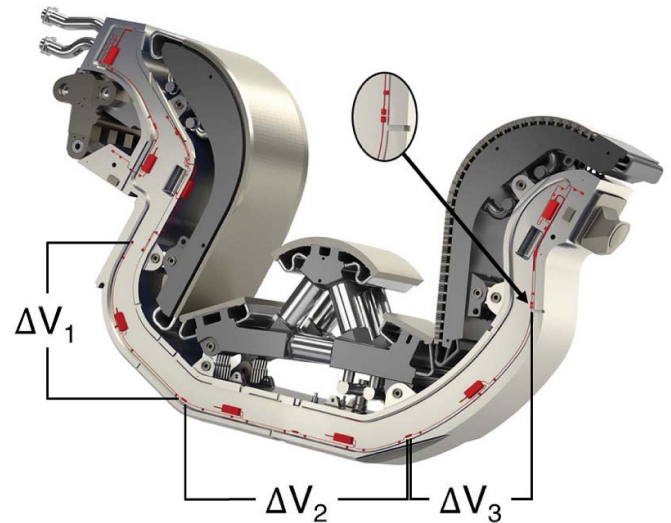
Figure 1. Render of the planned divertor shunts along the body of a ITER divertor cassette. Cable leads (shown here in red) run from 8 junction boxes (also in red) along the cassette body to 9 shunt test locations, forming 8 shunt pairs in total (shown the detailed view). The shunt voltage pairs relevant to SOL current measurements are labelled as ΔV_1, ΔV_2, and ΔV_3.

the ITER divertor, 6 uniformly distributed cassettes will be outfitted with the shunt diagnostic system (cassettes 5, 11, 23, 29, 41, 47). Though the SOL current measurement role was originally intended only to contribute to synthesis of the plasma shape, $q(r)$ profile, and the wall gap of the main plasma, it may also be a potentially very useful indicator of plasma detachment. This paper will demonstrate why.

The advantage of the shunts as a detachment diagnostic would be significant given the simplicity of the measurement. The shunts are remote from the plasma and thus not subject to the lifetime issues faced by sensors located much closer to the plasma (e.g. bolometers, pressure gauges and Langmuir probes), nor are they associated with the sophisticated optical systems required by spectroscopic diagnostics.

Langmuir probe measurements in the AUG tokamak [10] and in the Tokamak à Configuration Variable [11] demonstrate that the total SOL current in attached divertor conditions is dominated by the thermoelectric current. The electron temperature (T_e) asymmetry between the inner and outer divertor targets is the source of this current [11]. The difference in T_e at the plates drives electrons along the SOL field lines from the hotter (usually the outer) target to the colder (usually the inner) target [10]. Local current measured by shunts embedded in the outer target of AUG is found to be a good approximation of both the outer divertor target temperature and heat flux [9, 12]. Excellent detachment control using these tile shunt signals in conjunction with radiated power measurements using resistive foil bolometers in a feedback control loop with nitrogen (N) impurity injection has been achieved on AUG [13].

There are additional pressing distinctions between the tile shunt measurements on AUG and the divertor cassette shunt measurements foreseen on ITER. Unlike on AUG, the test points for each of the shunt pairs are located along the cassette

Table 1. SOLPS-ITER simulations used in the investigation of SOL current detachment behaviour. Unique IMAS shot and run numbers identify each individual simulation. PFPO-1 indicates 'Pre-Fusion Power Operation', the specifics of which are described in Park *et al* [14]. FPO simulations indicate 'Fusion Power Operation,' when $Q_{DT} = 10$ baseline operation at $P_{SOL} = 100$ MW should be achieved [1, 5]. All simulations use a top gas puff location.

IMAS Shot Number	Run	SOL Power (MW)	Species	Fluid Drifts	Scenario Summary
103 045–103 053	3	20	H	off	PFPO-1, H-puff $8.85 \times 10^{21} - 2.00 \times 10^{23}$ s^{-1} [14]
123 015, 123 017–123 019, 123 022*	3	100	D, He, Ne	on	FPO, $c_{Ne} < 0.8\%$, D-puff $1.00 \times 10^{23} - 1.95 \times 10^{23}$ s^{-1}, Ne-Puff $2.00 \times 10^{19} - 2.00 \times 10^{20}$ s^{-1} [5]
123 014, 123 016, 123 020, 123 021, 123 023–123 026	3	100	D, He, Ne	on	FPO, $c_{Ne} > 0.8\%$, D-puff $4.00 \times 10^{22} - 1.95 \times 10^{23}$ s^{-1}, Ne-Puff $1.00 \times 10^{19} - 1.00 \times 10^{20}$ s^{-1} [5]
123 1498– 123 155*	3	100	D, He, Ne	off	FPO, $c_{Ne} = 0.8\%$, D-puff $1.76 \times 10^{22} - 1.85 \times 10^{23}$ s^{-1}, Ne-puff $3.74 \times 10^{19} - 2.33 \times 10^{20}$ s^{-1}

*Cases are not explored here in detail, but are included in broader demonstration of detachment behaviour over an expanded range of plasma scenarios in section 3.1.

body rather than in the outer divertor target tiles, possibly introducing inertia in their response time. Another issue is that the AUG shunts measure the currents incident on the main tiles which intercept the strike points, whilst in the ITER system, it is the total current flow through the entire vertical divertor target which is measured. Lastly, the ITER divertor plasma is expected to behave differently to those on smaller devices in the sense that in-out divertor target asymmetries may be weaker under partially detached conditions [1, 5].

This paper will provide the first detailed analysis of the ITER divertor shunts as a detachment control diagnostic, assessing whether the shunt measurements accurately reflect the plasma detachment state. We first evaluate whether the total SOL current incident on the divertor target decreases as the divertor plasma transitions into a partially detached state. Next, we develop a lumped dynamic circuit model for the relevant divertor shunt pairs through electromagnetic finite element method (FEM) modelling of the impedance of the ITER divertor assembly. This circuit model, which is assessed for sensitivity and frequency response under expected operating conditions in ITER, is used to calculate SOL currents from shunt voltage measurements.

2. Methods

2.1. SOLPS-ITER simulations

To investigate the relationship between SOL currents and the divertor plasma state on ITER, we analyse data from various cases (sets of simulations) in the SOLPS-ITER plasma boundary simulation database, stored in the Integrated Modelling and Analysis Suite (IMAS) [14]. Some IMAS data

used in this paper is post-processed. The definitions of post processed variables, such as divertor neutral pressure p_n and Ne impurity concentration c_{Ne} may be found in [1]. The simulations used, listed in table 1, are restricted to existing SOLPS-ITER cases with scans of p_n, covering the transition from the attached outer target regime to partial detachment.

The SOLPS-4.3 simulation database used for the analysis in [1] cannot be deployed here. The physics model in SOLPS-4.3 assumes ambipolar flow and thus does not solve for the parallel currents which are needed to make an assessment of the SOL current measured by the shunt voltage taps. In contrast, SOLPS-ITER does compute the currents and, unlike SOLPS-4.3, includes the capability to run with fluid drifts activated. Switching drifts on improves the fidelity of the physics model, especially regarding impurity transport in the case of extrinsic seeding of radiating species. Several drift-activated cases for burning plasma conditions from a recent study reported in [5] will be used here (table 1, rows 2 and 3). They show similar trends to those found with SOLPS-4.3 [1], though the evolution of detachment behaviour with fuel throughput (or equivalently p_n) and the magnitudes of divertor asymmetries differ from the cases without drifts.

The first set of simulations we address (listed in the first row of table 1) is a pure hydrogen (H) fuelling scan at SOL power $P_{SOL} = 20$ MW appropriate to the conditions expected in the first non-active phase of ITER operation: PFPO-1 [14]. Drifts are not enabled in these simulations and they thus have the merit of being the simplest possible situation, with no impurities and in which there is essentially no contribution to the total SOL current other than that originating from thermoelectric effects. Figure 2 compiles the key divertor target quantities for the PFPO-1 simulations, showing the progression through
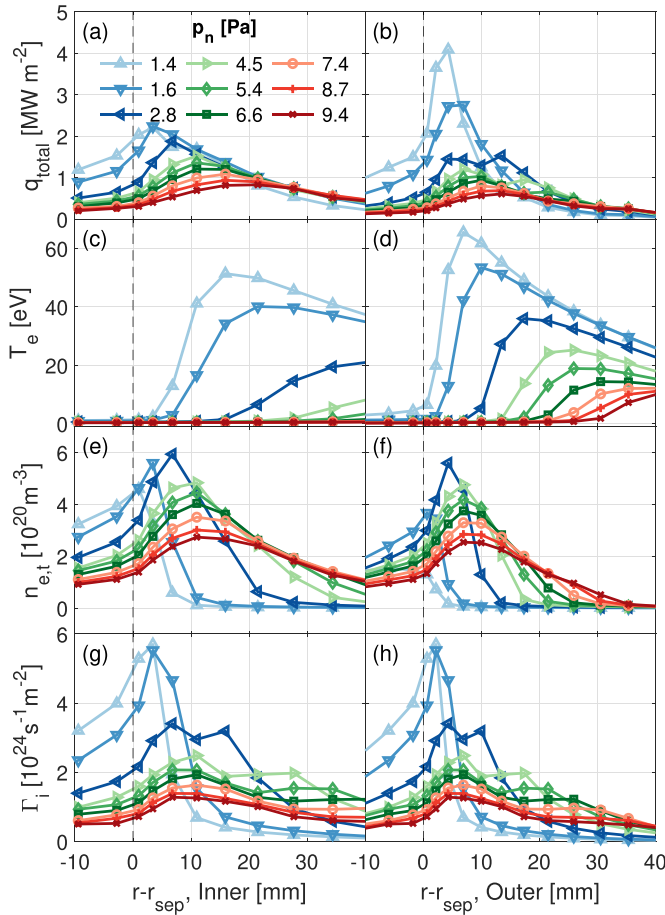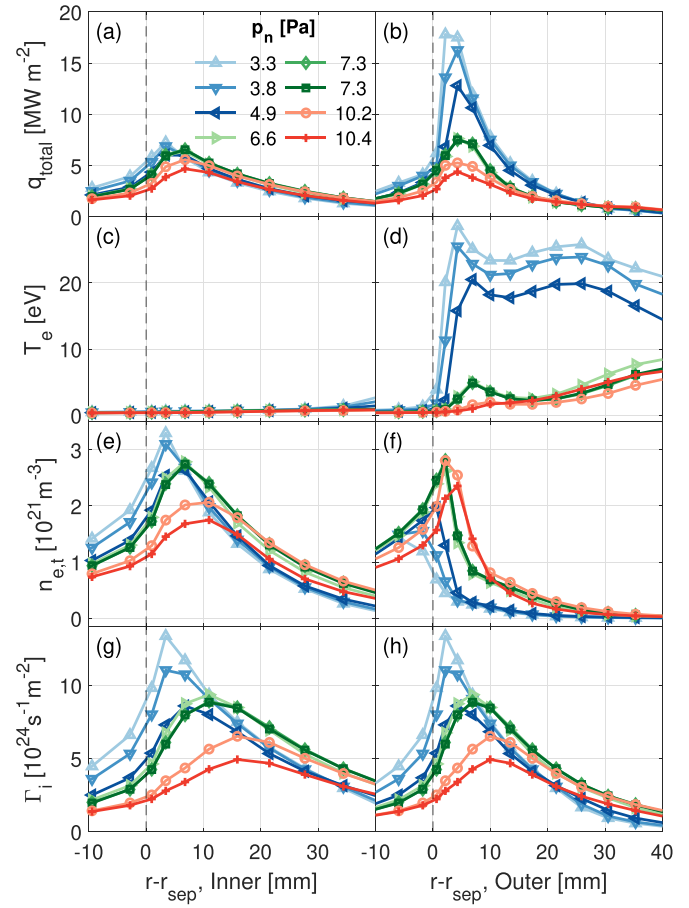
Figure 2. SOLPS-ITER divertor target profiles for the PFPO-1 pure H fuelling scan (see table 1 and [14]) (*a*), (*b*) total heat flux q_{total}, (*c*), (*d*) electron temperature T_e, (*e*), (*f*) electron density n_e, and (*g*), (*h*) ion flux Γ_i profiles for the inner and outer targets, respectively. Results are for the cylindrically symmetric case and therefore do not account for toroidal variation of the magnetic field line angle of incidence on the divertor target. The black dashed-line denotes the position of the separatrix strike point. The legend gives the divertor neutral pressure appropriate to each curve.

Figure 3. Equivalent of figure 2 for the SOLPS-ITER divertor target profiles for the FPO deuterium (*D*) fuelling scan with fluid drifts enabled for the inner and outer targets, respectively.

high-recycling to detached phases. In particular, one may note the gradual 'erosion' into the divertor SOL of the T_e profile with increasing p_n (corresponding to increasing gas fuelling rate), and the concomitant decrease in particle flux density, electron density, and target heat flux as detachment proceeds. A notable feature is the in-out T_e asymmetry, especially the more rapid decrease for given p_n at the inboard target. It is this asymmetry which primarily drives the thermoelectric current. At the highest p_n in this scan, T_e has essentially collapsed across almost the entirety of the inner and outer targets. Note, however, that at these low SOL powers, the divertor density is insufficient for any significant volumetric recombination to occur.

The detachment behaviour seen in figure 2 for the pure H throughput scan at low P_{SOL} may be contrasted with the situation under burning plasma (FPO) conditions ($P_{SOL} = 100$ MW), in which impurity seeding is mandatory to achieve detachment (in this case using Ne). This is shown in the divertor profiles in figure 3 for the higher power simulations in

Row 3 of table 1, comprising a fuel throughput scan where $c_{Ne} > 0.8\%$. The simulations include fluid drifts, which, as demonstrated in [5], significantly impact the detachment behaviour through their influence on the impurity transport in the divertor plasma. These simulations with drifts activated may thus be the most realistic model currently available of the ITER divertor plasma response to impurity seeding.

In general, the more complex, FPO case shows similar trends with increasing p_n to the PFPO-1 simulations. An obvious distinction between the low and high P_{SOL} cases is the stronger in-out asymmetry in T_e across the whole pressure range, as the inner target temperature is essentially collapsed across the whole plate. This is a notable consequence of the drifts, which convect impurities preferentially to the inboard divertor plasma, leading to a colder, denser plasma early on in the throughput scan. At the outboard divertor, T_e falls only at the highest p_n, though it should also be made clear that the c_{Ne} is not held constant through the throughput (and hence p_n) scan in this set of simulations. This is more challenging when fluid drifts are enabled, meaning the series of throughput scans at constant c_{Ne} in the SOLPS-4.3 simulation database [1] are not yet all available in the SOLPS-ITER database. To control for this variability, figure 3 only includes simulations where c_{Ne} exceeds 0.8%. We note also that, in comparison with the low

power PFPO-1 simulations, in these higher power drift runs, cases at very low p_n have not yet been achieved.

2.1.1. Contributions to the divertor plate currents. Essential to understanding the shunt diagnostic measurements is the physics underlying the current density in each flux tube which contributes to the overall integrated SOL current. Current in the SOL is understood to be, at least in part, driven by the temperature differential between the inner and outer divertor targets [11, 15, 16]. This phenomenon is called the thermo-electric effect. For diverted tokamak plasmas with the $B \times \nabla B$ ion drift direction towards the X-point, the inner divertor plasma is typically colder than the outer. Electrons flow along field lines from the cold to the hot target, driving a positive current from the outer divertor to the inner divertor [10]. Thermoelectric currents have, for example, been shown to dominate the total SOL current during stationary H-mode discharges on AUG under conditions in which Te at the outer target is higher than at the inner [9]. Additional current drive may arise from pressure gradients between the divertor targets along a given flux tube [17]. The thermoelectric effect is captured in an extension of Staebler and Hinton's 1D formulation for the SOL current density $j_\parallel$ along a given flux tube [17]:

$$j_\parallel = -\frac{\bar{\sigma}_\parallel T_c}{e L_\parallel} \left\{ k' \left(\frac{T_h}{T_c} - 1 \right) - \frac{1}{T_c} \int_c^h \frac{\nabla_\parallel p_e}{n_e} + \ln \left[\frac{1 + j_\parallel / j_{sC}}{\left(1 - \sqrt{\frac{T_h}{T_c}} \frac{j_\parallel}{j_{sC}} \right)^{T_h / T_c}} \right] \right\} \tag{1}$$

Along a given field line, Staebler and Hinton define j_{sC} as the parallel ion saturation current for the cold inner target, $\bar{\sigma}_\parallel$ as the average Spitzer conductivity parallel to the field line, $L_\parallel$ as the connection length, and T_c and T_h as the temperature at the cold inner and hot outer targets, respectively [17, 18]. The expression in equation (1) is not the form used in SOLPS-ITER. For detailed description of SOLPS-ITER model for currents in plasma see [19]. However, the formulations are equivalent when the coefficient k' in front of the temperature difference (first) term is properly adjusted to account both for the fact that the effect of the pressure gradient (second term)—which drives the pre-sheath potential fall—is already included in this term and that SOLPS-ITER as used to generate the cases considered in this paper assumes a fixed secondary electron emission coefficient of 0.5 in computing the sheath potential fall. The total effective resistance between the divertor targets along the cassette body (calculated in section 2.2) is $\sim 10 \mu\Omega$, limiting the potential drop along the cassette to ~ 10 mV. This low potential difference means that biasing due to resistivity of the divertor cassette will not impact the plasma solution.

The overall result (for $T_e = T_i$), when comparing the analytic result in equation (1) with SOLPS-ITER output, is a required value of $k' = 1.44$. Of course, differences are expected when comparing the numerical simulations with this expression due to the 2D nature of the code which also includes electric current exchange between adjacent flux tubes. Here, equation (1) is solved using a non-linear optimization function with non-linear constraints defined by the natural logarithm (third) term. The corresponding $j_\parallel$ value calculated by SOLPS-ITER on any given flux tube is supplied as an initial guess to account for sensitivity in the solution.

Current density $j_\parallel$ profiles for the analytical solution given in equation (1) (figure 4) agree reasonably well with the $j_\parallel$ profiles calculated by SOLPS-ITER for the pure H, PFPO-1 case without fluid drifts enabled. Further, the $j_\parallel$ peaks in both sets of profiles are consistent with the peak in T_h/T_c between the inner and outer divertor targets. Equation (1) cannot account for 2D transport between adjacent flux tubes, resulting in some discrepancy between the peak location of the analytical $j_\parallel$ and SOLPS-ITER $j_\parallel$ data. Nonetheless, the current along the SOL is clearly thermoelectric in nature. As p_n increases, the outer divertor begins to detach and the target temperatures equalise. The total SOL current is expected to decrease as a result.

The thermoelectric current contribution is less evident in $j_\parallel$ data at the divertor targets once fluid drifts and impurities are included in the simulation. SOLPS-ITER modelling with drifts includes all drift contributions and all non-negligible radial currents in the SOL and private flux region (PFR): the currents associated with ∇B drift of guiding centres, classical parallel viscosity, anomalous viscosity acting on the $E \times B$ rotation of the plasma, and that arising from drifts driven by ion friction with neutral atoms. For the high c_{Ne} FPO simulations with inclusion of fluid drifts, the SOLPS-ITER divertor target $j_\parallel$ shows little correlation with the T_h/T_c ratio as expressed in the analytic function of equation (1). Moreover, within the PFR, the current density profiles exhibit current drive in the opposite direction of the temperature gradient along each flux tube. As a consequence, the thermoelectric effect described in equation (1) cannot reconstruct the SOLPS-ITER current density profiles near the strike point.

The analysis of drift current contributions in the SOL and PFR shows that, beyond the thermoelectric current contribution, both plate closing currents (PCCs) compensating downward ∇B current [20–22] and parallel currents compensating neutral friction currents [22–24] contribute to the $j_\parallel$ profile along the divertor targets. We note for completeness that the well known Pfirsch–Schlüter parallel currents [23], which arise to short circuit ∇B and curvature drifts in the SOL above the X-point, do not make any significant contribution to the
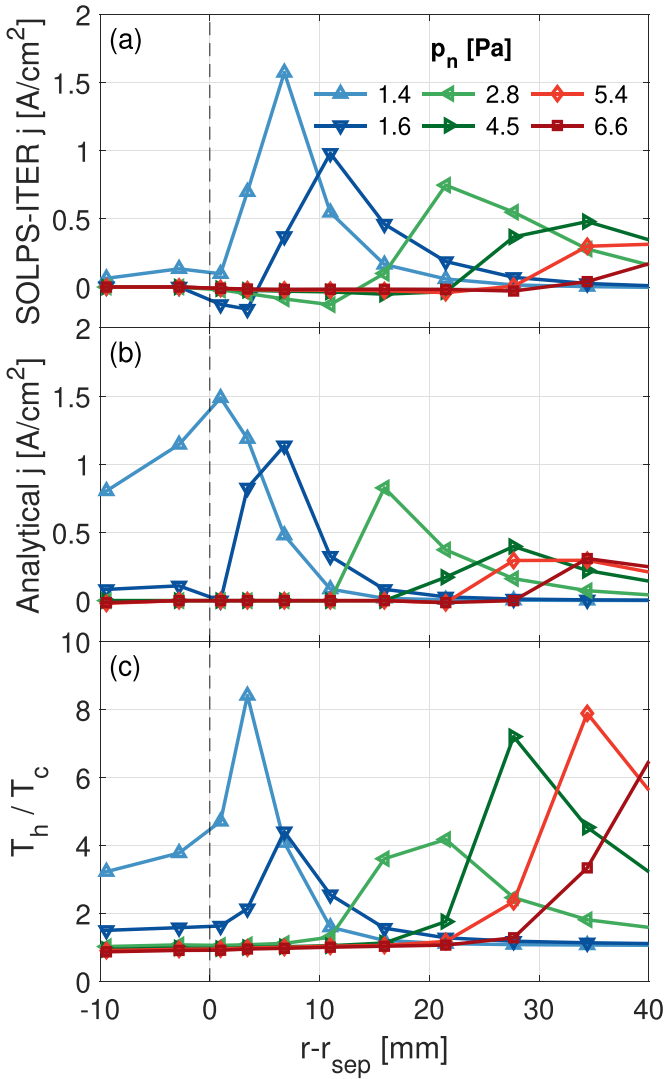
Figure 4. The (*a*) total $j_\parallel$ profile output from SOLPS-ITER and (*b*) $j_\parallel$ profile calculated with equation (1) compared to the (*c*) ratio of the hot outer divertor target temperature T_h to the cold inner divertor target temperature T_c near the separatrix (indicated by the black dotted line) for the pure *H* PFPO-1 throughput scan. All profiles are mapped to the outside midplane.

**Figure 5.** The drift currents circulating in the divertor region of the 10.4 Pa FPO simulation with fluid drifts enabled, extracted from SOLPS-ITER current data calculated for the entire divertor in the 2D poloidal plane. The inner and outer divertor targets are grey boxes on the left and right side of each diagram, respectively. The dashed green line represents the magnetic separatrix. Orange arrows indicate drift-driven currents, blue arrows the SOL and circuit-closing divertor currents, and the blue–orange gradient arrow denotes locations with a combination of both current contributions.

target integral current. They flow primarily in the hotter plasma with high electric conductivity near the separatrix and act simply as a modulation of the thermoelectric current without affecting the electrostatic potential distribution and the current flowing between the targets [21].

In contrast to the divergence-free thermoelectric current, the PCCs are closed by radial currents which arise due to the inclusion of fluid drifts in the simulation. Within the PFR, the $j_\parallel$ to the plate driven by these drift effects is in the opposite direction to the thermoelectric current. This is demonstrated in figure 5 for the simulation number 123 021 ($p_n = 10.4$ Pa) from the high c_{Ne} FPO series with drifts activated. The drift-driven current runs along the plasma near the surface of the divertor target and re-enters the divertor inside the PFR in the opposite direction to the thermoelectric current outside of the separatrix. These currents then run through their respective

divertor targets, re-entering the plasma outside the separatrix, completing 'plate-closing' current circuits. These drift-driven PCCs cancel themselves out when integrated over the entire plate, resulting in the total SOL current equalling that through the divertor cassette (SOLPS-ITER simulations are 2D and calculate the total, toroidally symmetric current flowing into all divertor targets) [21, 22]. The divertor shunt diagnostic only measures this integrated total SOL current and therefore is blind to the effects of the neutral-friction current and PCCs. Consequently, the remaining integrated current density that the shunt diagnostic measures is the thermoelectric current.

2.2. Circuit modelling of the ITER divertor

Reconstruction of the SOL current magnitude requires calculation of the current flowing through the divertor cassette from the voltage data measured by the ITER divertor shunts and an impedance model. For the purposes of the assessment reported here, the latter has been developed using an ANSYS® Q3D Extractor FEM model of the divertor assembly and shunt locations relevant to SOL current synthesis [25]. The model treats the cassette and SOL as a lumped inductor-resistor circuit
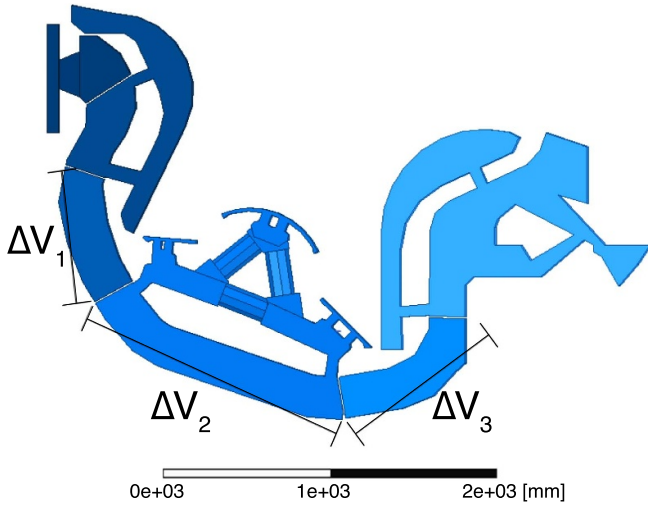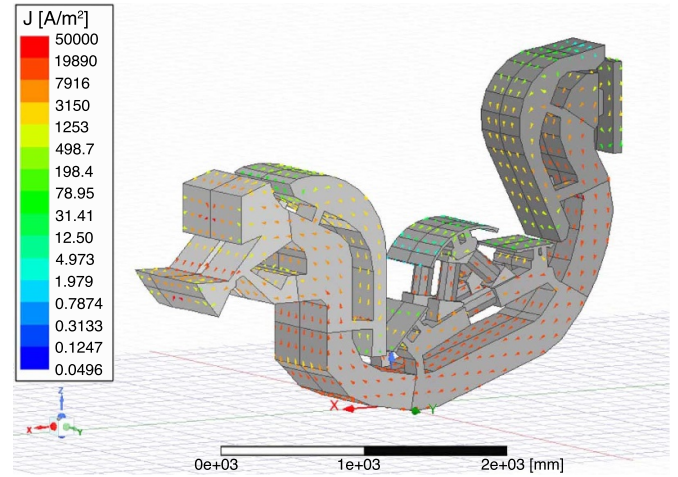
Figure 6. The reduced Q3D extractor model of the ITER divertor is physically split by a gap of several mm into virtual sections corresponding to the shunt lead test locations in figure 1. Each split location is then specified as the source or sink terminal FEM boundary condition for each conducting section. The impedance values output by the model solution are given in equations (3) and (4).

Figure 7. ANSYS® Maxwell electric transient FEM simulation of the simplified CAD model. About 1 kA is applied to the inboard vacuum vessel connection vessel surface and the outboard vacuum vessel connection is defined as the ground terminal. The field overlay for the peak $j_\parallel$ of the simulation demonstrates the path of current flow along the divertor cassette body.

with voltage nodes at each shunt test location. To validate this model, the voltage drop calculated along the cassette body is compared to values simulated in the ANSYS® Maxwell EM FEM software. We then use the calculated impedance values to assess the shunt diagnostic sensitivity and frequency response. Development of such a lumped circuit model would in any case be necessary for any future control system integration of the shunt diagnostic.

Previous FEM models of the ITER divertor yielded only the overall resistance of the divertor cassette assembly between connections to the vacuum vessel. The resistance between any two adjacent shunt test points was estimated to be $\sim 5\,\mu\Omega$. The divertor shunt taps in figure 1 were located to reflect major current ingress and egress points identified in that analysis. Our new analysis seeks to extend this work by calculating the impedance between shunt measurements, which requires dividing a CAD model of the divertor into virtual sections based on the location of the relevant divertor shunt taps (figure 6). The model simplifies the detailed CAD assembly of the ITER divertor cassette by approximating complex cooling and structural geometries as tetrahedra of equal cross-sectional area, maintaining the effective conductivity of the structure. In the ANSYS® Q3D Extractor program, each section is designated as a conducting body whose source and sink terminals are the adjacent sections.

The Q3D FEM solution calculates a resistance matrix R and inductance matrix M for the divertor cassette (equations (3) and (4)). FEM model convergence of 0.1% relative error is achieved through adaptive mesh refinement of 30% per solution iteration. The M and R matrices govern the coupling between each voltage drop measured by an individual shunt pair along each section of the divertor cassette. The voltage shunt pair measurements are denoted in figure 6 by ΔV_1, ΔV_2,

and ΔV_3 and correspond to the current flowing though each divertor section. The relationship (2) between the measured shunt voltages and the M and R matrices is captured by the state space format that is common in control engineering:

$$\dot{I} = -M^{-1}RI + M^{-1}V$$
$$V = [\Delta V_1 \; \Delta V_2 \; \Delta V_3] \qquad (2)$$
$$I = [I_1 \; I_2 \; I_3]$$

$$R = \begin{bmatrix} 8.64 & 0 & 0 \\ 0 & 12.8 & 0 \\ 0 & 0 & 7.77 \end{bmatrix} [\mu\Omega] \qquad (3)$$

$$M = \begin{bmatrix} 198 & 79.3 & -10.3 \\ 79.3 & 480 & 68.7 \\ -10.3 & 68.7 & 206 \end{bmatrix} [\text{nH}]. \qquad (4)$$

To address the concern that the virtual division of the divertor cassette body into several sections would alter the conducting behaviour of the model, the Q3D Extractor solution is verified against an EM simulation in ANSYS® Maxwell. A 1 kA current excitation is applied to the inboard vacuum vessel connection vessel surface. The outboard vacuum vessel connection is defined as the ground terminal. The voltages at each relevant shunt test location are recorded (figure 7). Similarly, 1 kA is applied as the input current vector I to the circuit equation given in equation (2). The differences between the total voltage drop across all three shunt pairs as calculated in equation (2) and the voltages output by the Maxwell simulation shunt locations are found to be consistently within <1%. This then confirms that the Q3D impedance values are valid within the context of the given FEM model.

The SOLPS-ITER simulations used here are time independent, stationary solutions, representing the divertor plasma state for given input parameters. As such, they can map-out the range of detachment behaviour, but do not provide any indication of time dependent response. Reattachment dynamics are dependent on divertor Ne residence times and are predicted evolve over a timescale of ~ 0.1 s [26]. Direct measurements of the as-built physical divertor cassette impedance taken using both DC excitation and a detachment-relevant range of AC excitation frequencies are planned to improve model accuracy. However, because reattachment dynamics are predicted to be slow (relative to time scales of current skin effects), the DC resistance values offer reasonable estimates on which to conduct diagnostic sensitivity analysis.

3. Results

3.1. SOL currents in detaching plasmas

Since the divertor cassette body completes a poloidal circuit with the SOL, the current measured by the divertor shunts can be assumed to capture the total net current flow computed in 2D by SOLPS-ITER. In what follows, we use divertor neutral pressure (p_n), which in the SOLPS-ITER simulations increases during the progression to detachment (see figures 2, 3 and [1, 7, 8, 12, 27]), as a zero-dimensional proxy for detachment onset.

Beginning with the PFPO-1 scenario simulations (2), figure 8 plots the total current incident on the inner divertor against p_n. The integral current falls steeply (a factor 10 decrease) from 7.8 kA at the lowest p_n to 0.6 kA for the most strongly detached case in the scan. The picture is similar for the higher P_{SOL} FPO cases. When compared with a set of SOLPS-ITER FPO runs without drifts (last row in table 1), the absolute integral current values are higher when drifts are included, but the trends are the same. For each of the cases included in figure 8, the scan of p_n always results in a decrease in total incident current (of order kA) regardless of simulation-specific parameters.

It is clear from figure 8 that at high p_n, when divertor targets are rather detached (figures 2 and 3), the total simulated current varies widely for the different simulation groups. The physical parameters controlling the divertor conditions (and thus the in-out divertor plasma asymmetries and the currents between the target plates) are P_{SOL}, p_n and the concentration of radiating impurities (the type of extrinsic impurity and the fuelling injection location also play a role). They also dictate the outer target heat load, which, for lower p_n (when the loads can rapidly exceed the stationary power handling limits on ITER) is always the highest of the two targets (figures 2 and 3) in the SOLPS-ITER modelling (and generally in experiments on current devices). This heat load, or, in practice, the target surface temperature, is therefore the critical parameter to control. Hence, the key question is whether there exists a correlation between the target heat load and the shunt current.

As shown in figure 9, such a correlation clearly exists between the integral target current to the inner divertor and the peak outer target heat flux for all the SOLPS-ITER simulation
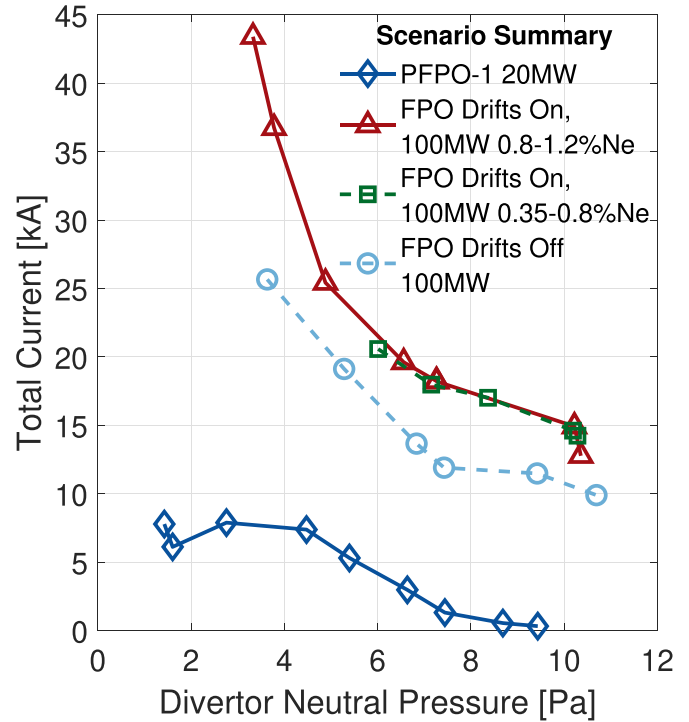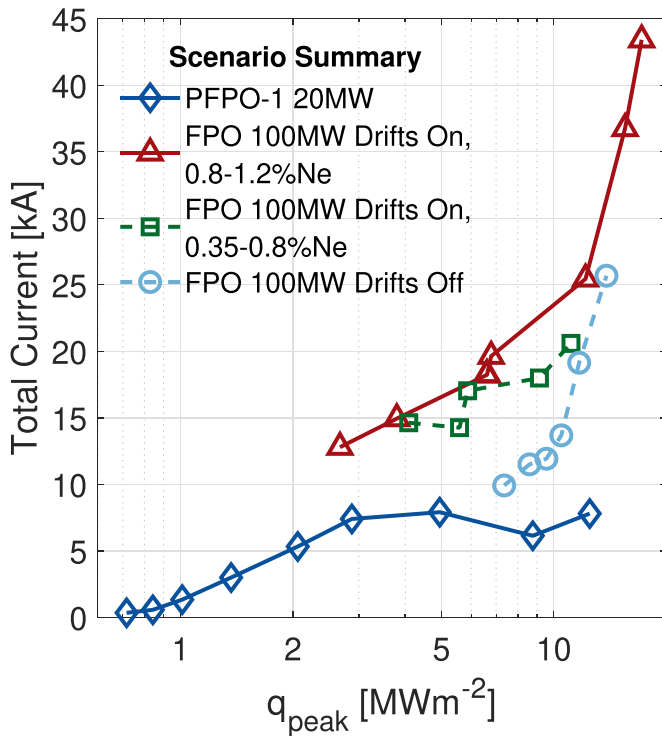
Figure 8. Dependence of the total current to the inner target on p_n for the SOLPS-ITER simulation cases in table 1.

cases in table 1. It is, therefore, not a straightforward question of whether or not the shunt diagnostic measures a pure temperature difference (the simulations shown here demonstrate that it likely does not), or whether it can distinguish clear 'detachment states', but more whether this system, one of the simplest of the various being installed in ITER, can contribute to solving the general issue of power load control. Figure 9 provides some hope that a transfer function between the current measured and the peak heat load might eventually be derived. In practice, this will only be possible once experiments begin and real shunt measurements can be compared with those of the peak heat loads.

To conclude this section, it is worth pointing out that the analysis here, being restricted to 2D, time independent SOLPS-ITER simulations, takes no account of the possible fast transient target heat loads due to Edge Localized Modes (ELMs), nor potential 3D effects. Regarding the ELMs, it is generally assumed that, in these static plasma boundary simulations, the majority of the power they bring into the SOL (which is in the range $\sim 20\%$–40% of P_{SOL} for Type I ELMs [28]) is deposited roughly in the same location as the inter-ELM power flux (namely at the strike points). On ITER, unmitigated Type I ELMs will not be tolerable in burning plasma regimes. Mitigation systems, in particular the use of in-vessel magnetic coils to apply magnetic perturbations (MPs), are foreseen [29].

The ITER ELM mitigation system aims for complete ELM suppression, but with a mitigation target (to avoid surface melting of the divertor W monoblock top surfaces) of ≈ 0.9 MJ m^{-2} for the peak perpendicular ELM energy density at the divertor plates [1]. This corresponds to ELM frequencies

Figure 9. Dependence of the total current to the inner target on the peak heat flux to the outer plate for all the SOLPS-ITER simulation cases in table 1.

of several tens of Hz and to energy losses per ELM which will be largely sufficient to burn through any detached divertor plasma. Each ELM event can be assumed to briefly (on the millisecond timescale) raise T_e at the target plates to values characteristic of the H-mode pedestal temperature [30]. Indeed, a model consistent with the recent scaling of experimental outer target parallel ELM energy densities treats the ELM event as a brief reconnection of the pedestal plasma to the divertor targets [31]. Under such conditions, it is not clear how much thermoelectric current would be driven by the ELM event.

Unfortunately, there are almost no observations of ELM driven thermoelectric currents on current devices. The study in [11], for rather benign Type III ELMs, found evidence for at least some thermoelectric component of ELM target currents. What is clear, as the analysis in the following section will demonstrate (figure 10), is that the ITER shunt diagnostic will not be capable of discriminating ELM driven currents since the tap voltage drops decrease rapidly for events at frequencies expected for mitigated ELMs. However, for millisecond transients at frequencies of several tens of Hz, only small fractions of any given time period will correspond to non-inter ELM phases. We thus believe that the analysis presented here will remain broadly correct in terms of the relative response of the diagnostic to the detachment state based on pure stationary SOLPS-ITER simulations.

Furthermore, the question of 3D effects remains open. Recent studies of the impact of MPs on the ITER divertor

plasma using the EMC3-Eirene plasma boundary solver [32] clearly show how the perturbations lead to non-axisymmetric 'lobes' of target power deposition, in which plasma characteristic of the pedestal region can reach the divertor plates. Moreover, detachment of power fluxes in these regions of enhanced power flux may prove challenging. At present, the database of these extremely complex simulations is rather restricted, especially under burning plasma conditions, and the capabilities of EMC3-Eirene (for which the simulations do not include drifts or currents) do not yet permit assessment of the thermoelectric currents.

3.2. Circuit modelling sensitivity and frequency response

We may now combine the analyses in sections 2 and 3.1 to analyse the sensitivity of the diagnostic to the expected SOL current magnitude and the frequency response of the shunt measurement to a changing SOL current. Beginning with steady state sensitivity, the divertor shunts have an expected absolute signal accuracy of 0.1 mV and relative signal accuracy of 3.5%. Equation (3) gives the minimum resistance of the divertor cassette section between the relevant shunt pairs as $7.77 \mu\Omega$. The fully saturated DC resistance measurement estimates a conservatively low resistance of the lowest impedance section of the divertor cassette. This divertor section resistance yields a minimum detectable divertor cassette current of 13 A. Multiplied across 54 divertor cassettes, the divertor shunt diagnostic would be able to detect minimum SOL currents on the order of 0.1 kA. Only the two lowest current values from the SOLPS-ITER PFPO-1 scenario simulations fail to meet this lower limit.

Utilising calculated impedance values (equations (3) and (4)) input into equation (2), transfer functions are computed between the current flowing through each section of the divertor cassette and the shunt lead pair affixed to each of those sections. For the purpose of this analysis, we define the input to the state space model as a vector with the voltage measured on each of the section's boundaries and the output as the current entering and exiting those boundaries.

The resulting frequency analysis describes how the shunt voltage signal responds to changes and transients in the SOL current. The frequency response of this state space system from 0.1–100 Hz in figure 10, encompasses the range of all frequencies that this sensor system would measure. In the low frequency range (0.1–10 Hz), the voltage signal shows very high gain against SOL current of approximately 100 dB due to the low resistance of the cassette across all three shunt lead pairs in figures 10(*a*)–(*c*). While the inductive response of each of the shunt pair voltages peaks between 1–10 Hz, it is always at least 10 dB lower than the response to resistance. Finally, for low frequency voltage signals, the current signal has little to no phase lag to the current in figures 10(*d*)–(*f*). At higher frequencies, as indicated by the drop in phase, the signal begins to lag as the inductive mutual coupling counters changes in the voltage.

Inner Shunt ΔV$_1$　**Center Shunt ΔV$_2$**　**Outer Shunt ΔV$_3$**
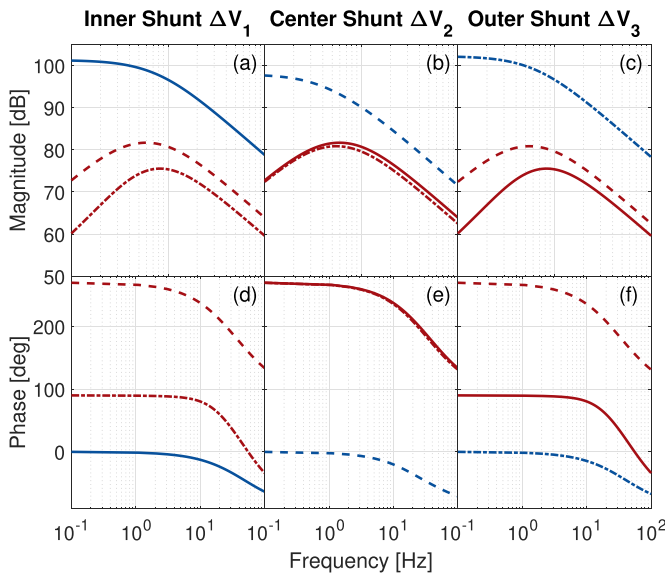
Figure 10. Bode plots of the frequency response of equation (2) to a sinusoidal current from 0.1–100 Hz for the three shunt lead pairs specified in figure 1. The plots are separated into the frequency response to current through the shunt pair on the inboard side of the divertor cassette (I_1, solid line —), current through the shunt pair in the centre of the divertor cassette (I_2, dashed line —), and current through the shunt pair on the outboard side of the divertor cassette (I_3, dashed-dotted line ···). For each plot, the resistance response to the current through the given shunt pair is shown in blue, with the inductance response of the shunt pair to current through the other two shunt pairs given in red.

4. Discussion and conclusions

In this paper, we identify a correlation between the magnitude of the SOL current measured by the voltage tap shunts which will be installed on the cassette bodies of several of the divertor units on ITER and the onset of partial detachment, derived from the database of SOLPS-ITER plasma boundary code simulations. A lumped circuit model of the divertor cassette is then used to calculate the SOL current from the voltages measured by the shunt diagnostic. We then evaluate the performance of the diagnostic in terms of sensitivity and system frequency response.

Several key insights can be deduced from the analysis of the expected SOL currents. The total currents incident on the ensemble of divertor targets are in the range of kA for the lower power discharges which will characterize early, non-active operation on ITER and tens of kA for baseline $Q_{DT} = 10$ burning plasma operation in the nuclear phase. In fuel throughput scans, in which the divertor neutral pressure increases, these currents decrease consistently with increasing levels of divertor detachment. We observe a strong correlation between the reduction in current flowing through the SOL and the reduction of peak heat flux incident on the outer divertor target. These two relationships are stronger when fluid drifts are included in the SOLPS-ITER simulations. Ultimately, only experiments on ITER itself will determine whether target heat fluxes can indeed be correlated with the integral target currents that the planned shunt diagnostic measures. Nevertheless, our analysis

demonstrates that this rather simple diagnostic could plausibly be used in this way even if it was not originally designed for the purposes of detachment or outer target power flux control. It should certainly be counted amongst the potential group of sensors to be deployed on ITER which may be used by the plasma control system to achieve control objectives.

With regard to diagnostic sensitivity, if the current-per-cassette falls below approximately 13 A, divertor shunts may be unable to sense variation after the onset of partial detachment. Yet, the absolute necessity for detachment control is only relevant to the high powers which will be experienced during burning plasma operation on ITER. Our modelling shows that ITER is unlikely to approach the sensitivity floor under such conditions. Sensitivity, therefore, will not be of concern when detachment control is absolutely crucial to divertor target survival.

From the perspective of synthetic control diagnostic development, each shunt lead pair will see high current gain for relevant frequency ranges. The current driven by inductance is consistently an order of magnitude lower than the ohmic current. Furthermore, the diagnostic bandwidth encompasses signals within transient reattachment timescales (0.1–1 s [26]). Based on the relatively low magnitude of the inductance signal, the inductive mutual coupling effects could possibly be neglected entirely. Additionally, excitation measurements of the physical divertor assembly will be necessary to measure accurate AC resistance values. The measurements of such a study would then replace the simulated R and M matrices in the equation (2) lumped circuit model.

ORCID iDs

C.A. Orrico ⓘ https://orcid.org/0000-0001-8522-0974
T. Ravensbergen ⓘ https://orcid.org/0000-0001-7347-5515
R.A. Pitts ⓘ https://orcid.org/0000-0001-9455-2698
E. Kaveeva ⓘ https://orcid.org/0000-0002-8283-9138
J.S. Park ⓘ https://orcid.org/0000-0003-0871-7527
I. Senichenkov ⓘ https://orcid.org/0000-0001-5458-4919

References

[1] Pitts R.A. *et al* 2019 Physics basis for the first ITER tungsten divertor *Nucl. Mater. Energy* **20** 100696
[2] Escourbiac F., Durocher A., Fedosov A., Hirai T., Pitts R.A., Gavila P., Riccardi B., Kuznetcov V., Volodin A. and Komarov A. 2019 Assessment of critical heat flux margins on tungsten monoblocks of the ITER divertor vertical targets *Fusion Eng. Des.* **146** 2036–9

[3] Krasheninnikov S.I. and Kukushkin A.S. 2017 Physics of ultimate detachment of a tokamak divertor plasma *J. Plasma Phys.* **83** 155830501

[4] Loarte A. and Neu R. 2017 Power exhaust in tokamaks and scenario integration issues *Fusion Eng. Des.* **122** 256–73

[5] Kaveeva E. *et al* 2020 SOLPS-ITER modelling of ITER edge plasma with drifts and currents *Nucl. Fusion* **60** 046019

[6] Janeschitz G., Borrass K., Federici G., Igitkhanov Y., Kukushkin A., Pacher H.D., Pacher G.W. and Sugihara M. 1995 The ITER divertor concept *J. Nucl. Mater.* **220–222** 73–88

[7] Boedo J., McLean A.G., Rudakov D.L. and Watkins J.G. 2018 A review of direct experimental measurements of detachment *Plasma Phys. Control. Fusion* **60** 044008

[8] Ravensbergen T. 2021 Advanced methods in control of the core density and divertor detachment in nuclear fusion devices *PhD Thesis* Mechanical Engineering

[9] Kallenbach A. *et al* 2010 Divertor power load feedback with nitrogen seeding in ASDEX Upgrade *Plasma Phys. Control. Fusion* **52** 055002

[10] Kallenbach A., Carlson A., Pautasso G., Peeters A., Seidel U. and Zehrfeld H.P. (ASDEX Upgrade Team) 2001 Electric currents in the scrape-off layer in ASDEX Upgrade *J. Nucl. Mater.* **290–293** 639–43

[11] Pitts R.A., Alberti S., Blanchard P., Horacek J., Reimerdes H. and Stangeby P.C. 2003 ELM driven divertor target currents on TCV *Nucl. Fusion* **43** 1145–66

[12] Leonard A.W. 2018 Plasma detachment in divertor tokamaks *Plasma Phys. Control. Fusion* **60** 044001

[13] Kallenbach A., Bernert M., Eich T., Fuchs J.C., Giannone L., Herrmann A., Schweinzer J. and Treutterer W. (ASDEX Upgrade Team) 2012 Optimized tokamak power exhaust with double radiative feedback in ASDEX Upgrade *Nucl. Fusion* **52** 122003

[14] Park J.S., Bonnin X. and Pitts R. 2020 Assessment of ITER divertor performance during early operation phases *Nucl. Fusion* **61** 016021

[15] Harbour P.J. *et al* 1989 The X-point scrape-off plasma in JET with L-and H-modes *J. Nucl. Mater.* **162-164** 236–44

[16] Stangeby P.C. 2000 *The Plasma Boundary of Magnetic Fusion Devices* (New York: Taylor & Francis)

[17] Chankin A.V., Clement S., De Kock L., Erents S.K., Harbour J. and Tagle J.A. 1992 Parallel currents in the scrape-off layer of jet diverted discharges *J. Nucl. Mater.* **196–198** 739–44

[18] Staebler G.M. and Hinton F.L. 1989 Currents in the scrape-off layer of diverted tokamaks *Nucl. Fusion* **29** 1820

[19] Rozhansky V., Kaveeva E., Molchanov P., Veselova I., Voskoboynikov S., Coster D., Counsell G., Kirk A. and Lisgo S. 2009 New B2SOLPS5.2 transport code for h-mode regimes in tokamaks *Nucl. Fusion* **49** 025007

[20] Rozhansky V., Kaveeva E., Senichenkov I. and Vekshina E. 2018 Structure of the classical scrape-off layer of a tokamak *Plasma Phys. Control. Fusion* **60** 035001

[21] Rozhansky V., Kaveeva E., Senichenkov I., Sorokina D., Vekshina E., Coster D., McCarthy P. and Khromov N. (ASDEX Upgrade Team) 2020 Currents structure in the scrape-off layer of a tokamak *Nucl. Mater. Energy* **25** 100840

[22] Rozhansky V., Kaveeva E., Senichenkov I., Sorokina D., Vekshina E., Coster D., McCarthy P. and Khromov N. 2020 Current structure in the scrape-off layer of a tokamak in a quiescent state *Plasma Phys. Control. Fusion* **63** 015012

[23] Rozhansky V., Kaveeva E., Voskoboynikov S., Coster D., Bonnin X. and Schneider R. 2003 Potentials and currents in the edge tokamak plasma: simplified approach and comparison with two-dimensional modelling *Nucl. Fusion* **43** 614–21

[24] Ballester J.L. *et al* 2018 Partially ionized plasmas in astrophysics *Space Sci. Rev.* **214** 58

[25] Ansys® 2021 *R2 Electronics Desktop* (Natick, MA: Ansys, Inc.)

[26] Bonnin X., Pitts R.A., Komarov V., Escourbiac F., Merola M., Bo L., Wei L., Pan L. and Kukushkin A.S. 2017 ITER divertor plasma response to time-dependent impurity injection *Nucl. Mater. Energy* **12** 1100–5

[27] Stangeby P.C. 2018 Basic physical processes and reduced models for plasma detachment *Plasma Phys. Control. Fusion* **60** 044022

[28] Loarte A. *et al* 2003 Characteristics of type I ELM energy and particle losses in existing devices and their extrapolation to ITER *Plasma Phys. Control. Fusion* **45** 1549

[29] Loarte A. *et al* 2014 Progress on the application of ELM control schemes to ITER scenarios from the non-active phase to DT operation *Nucl. Fusion* **54** 033007

[30] Horacek J. *et al* (JET Contributors and COMPASS Team) 2023 ELM temperature in JET and Compass tokamak divertors *Nucl. Fusion* **63** 056007

[31] Eich T., Sieglin B., Thornton A.J., Faitsch M., Kirk A., Herrmann A. and Suttrop W. 2017 ELM divertor peak energy fluence scaling to ITER with data from JET, mast and ASDEX Upgrade *Nucl. Mater. Energy* **12** 84–90

[32] Frerichs H., Bonnin X., Feng Y., Li L., Liu Y.Q., Loarte A., Pitts R.A., Reiter D. and Schmitz O. 2021 Divertor detachment in the pre-fusion power operation phase in ITER during application of resonant magnetic perturbations *Nucl. Fusion* **61** 126027